Stress conditions for the propagation of discrete compaction bands in porous sandstone

Sheryl Tembe,[1] Patrick Baud,[2] and Teng-fong Wong[1]

[1]   Compaction bands are a compactant failure mode in porous rock, forming thin tabular structures normal to the maximum compressive stress with negligible shear offset. We investigated the conditions involved in the development of compaction bands in sandstone, including the influence of composition and the geometric attributes of the bands across a range of length scales. To extend beyond existing laboratory data on the relatively pure quartz Bentheim sandstone, a suite of triaxial experiments were conducted on Diemelstadt and Bleurswiller arkoses. Mechanical data and microstructural observations demonstrate that compaction bands can develop in compositionally heterogeneous rock and are the dominant failure mode in the transitional regime from brittle faulting to cataclastic flow. Synthesis of field and laboratory data on band dimensions in five sandstones over four orders of magnitude revealed a quadratic scaling relation between the thickness and length of compaction bands, wherein thickness is proportional to the square root of the band length. Using an anticrack/antidislocation fracture mechanics model, we obtained a scaling relation in which the stress level is inversely proportional to band thickness. We show that this relation provides a mechanical basis for interpreting discrepancies between laboratory and field data. Together, the laboratory and field data constrain the critical strain energy release rate in the model to be on the order of $2-80$ kJ/m^2, comparable with laboratory measurements.

Citation: Tembe, S., P. Baud, and T.-f. Wong (2008), Stress conditions for the propagation of discrete compaction bands in porous sandstone, *J. Geophys. Res.*, *113*, B09409, doi:10.1029/2007JB005439.

1.   Introduction

[2]   Strain localization is a pervasive phenomenon in the Earth's crust. It occurs over a broad spectrum of length scales, ranging from centimeter-sized laboratory samples up to crustal fault zones extending over hundreds of kilometers. Two modes of strain localization that have been widely investigated are shear and extensile discontinuities in the forms of faults and joints. A third mode of strain localization manifested by compaction band formation in porous clastic rocks is of recent interest. First documented in the field [*Hill*, 1989; *Mollema and Antonellini*, 1996], this compaction localization phenomenon has recently been explored in a number of theoretical and laboratory studies [e.g., *Olsson*, 1999; *Olsson and Holcomb*, 2000; *Issen and Rudnicki*, 2000; *Wong et al.*, 2001; *Baud et al.*, 2004; *Louis et al.*, 2006; *Fortin et al.*, 2006].

[3]   As a kinematic end-member of strain localization, compaction bands are planar structures that have undergone inelastic compaction predominantly due to shortening in a direction subperpendicular to their planar surface with negligible shear offset. In the field such compaction bands have been observed in the Aztec sandstone from Valley of Fire, Nevada [*Hill*, 1989; *Sternlof et al.*, 2005] and in the Navajo sandstone of the Kaibab Monocline, Utah [*Mollema and Antonellini*, 1996]. These tabular zones of compaction typically have thickness on the order of $1-10$ mm and trace lengths on the order of $1-10$ m.

[4]   Laboratory studies have detailed the development of compaction localization in sandstones with porosities ranging from 13% to 28% [*Olsson and Holcomb*, 2000; *DiGiovanni et al.*, 2000; *Klein et al.*, 2001]. Compactant failure at stress states in the transitional regime from brittle faulting to cataclastic flow often develops in a localized manner [*Wong et al.*, 2001], manifested by failure modes associated with a broad spectrum of geometric complexity [*Baud et al.*, 2004]. On the basis of acoustic emission (AE) and microstructural observations in centimeter-sized samples once localization is initiated, the primary mode of accommodating further compaction is by the initiation of additional discrete bands that remain relatively narrow, with thicknesses of about twice the grain diameter [*Klein et al.*, 2001; *Wong et al.*, 2001; *Fortin et al.*, 2006]. Significant reductions of permeability have been observed while compaction bands develop in a porous sandstone sample [*Holcomb and Olsson*, 2003; *Vajdova et al.*, 2004].

[5]   In many respects, the geometric attributes of discrete compaction bands as observed in the laboratory are morphologically similar to compaction bands that have been documented in the field. Notwithstanding these similarities,

[1]Department of Geosciences, State University of New York at Stony Brook, Stony Brook, New York, USA.
[2]Institut de Physique du Globe (CNRS/ULP), Strasbourg, France.

Sternlof et al. [2005] recently emphasized that there are at least two apparent discrepancies between the failure modes and structures observed in the laboratory and in the field. First, the stress level for compaction band formation that they inferred in the Valley of Fire is lower than that required in the laboratory for the development of discrete compaction bands. Second, the dimensions (thickness and length) as well as the damage intensity they measured in the field seem appreciably lower than those in the laboratory deformed samples. Indeed, such apparent discrepancies led *Sternlof et al.* [2005] to suggest that the experimental phenomenon may be largely unrelated to natural compaction localization.

[6] If the laboratory measurements can be realistically extrapolated to geologic settings, the mechanical basis for scaling of compaction band dimensions, stress state and damage should first be established. In this study we attempt to address this question by conducting complementary experiments to obtain a more comprehensive database, synthesizing all the laboratory data and incorporating recent theoretical advances. The most comprehensive investigation of discrete compaction band formation has been on Bentheim sandstone [*Klein et al.*, 2001; *Wong et al.*, 2001; *Baud et al.*, 2004], and indeed the stresses involved in experimental deformation of this porous sandstone with 95% quartz were at levels of several hundred MPa, an order of magnitude higher than those inferred for the field setting. In the presence of a structural heterogeneity in a circumferentially notched sample [*Vajdova and Wong*, 2003; *Tembe et al.*, 2006], the stress level for the initiation of discrete compaction bands was observed to be lower, but by less than an order of magnitude. In contrast, significantly lower stresses of several tens of MPa were recently reported by *Fortin et al.* [2006], who used AE measurement to characterize the progressive development of discrete compaction bands in Bleurswiller sandstone, an arkose with ∼50% quartz. An objective of the present study is to obtain complementary mechanical data on the Diemelstadt sandstone, which develops discrete compaction bands at stress levels between those for the Bentheim and Bleurswiller sandstones. The influence of water on its yield stress and failure mode was investigated by systematic comparison of the behaviors in saturated and nominally dry samples. Since *Fortin et al.* [2005, 2006] only investigated saturated samples, we conducted selected experiments on both dry and saturated samples of Bleurswiller sandstone to characterize the influence of water on its mechanical behavior.

[7] Recent studies have characterized quantitatively geometric attributes of the discrete compaction bands in laboratory deformed samples. *Louis et al.* [2006] has developed a technique whereby attributes such as band angle and tortuosity can be inferred from X-ray CT images. The band widths of Bentheim, Diemelstadt, and Bleurswiller sandstones were determined from our microstructural observations; in addition those of Bleurswiller sandstone can also be inferred from the AE data of *Fortin et al.* [2006]. The extensive database on geometry of compaction bands open up the possibility of a systematic comparison with the field data in the Aztec and Navajo sandstones in the two field areas in Nevada and Utah [*Hill*, 1989; *Mollema and Antonellini*, 1996; *Sternlof et al.*, 2005]. We will synthesize the field and laboratory data to underscore that the thickness and length of compaction bands seem to obey a quadratic scaling relation, which raises the question what the mechanical basis for such a scaling relation is. In a recent analysis *Rudnicki* [2007] formulated several models for compaction band propagation, and in particular he proposed a combined "anticrack/dislocation" model which would indeed result in the quadratic scaling we have identified in the field and laboratory data. With reference to this particular model, we will analyze the stress states associated with compaction band propagation and compare with the field and laboratory data.

2. Mechanical Data and Failure Modes of Diemelstadt and Bleurswiller Sandstones

2.1. Sample Description

[8] The Diemelstadt is a fluvial arkosic sandstone belonging to the Buntsandstein formation in central Germany. The samples were from the same block studied by *Baud et al.* [2004] and *Klein and Reuschlé* [2004] and its petrophysical properties are given in Table 1. Our samples were cored perpendicular to the sedimentary bedding and then ground to obtain cylinders with a diameter of 18.4 mm and length of 38.1 mm. Initial porosity of the samples used in this study range from 23.0% to 25.3% with a mean value of 24.3%. Microstructural observations indicate subparallel sequences of relatively fine grained laminae embedded in relatively coarse grained layers. The degree of inhomogeneity varies among the samples even though they were cored from the same block, and accordingly the mechanical behavior was not very reproducible for samples deformed under similar pressure conditions.

[9] The Bleurswiller sandstone is a grey arkosic sandstone (Table 1) from the Vosges mountain in France. Our samples were cored perpendicular to the sedimentary bedding and is from the same block described by *Fortin et al.* [2005, 2006]. We will also compare our data with those of Bentheim sandstone. This sandstone from Germany is very strong and quartz-rich sandstone (Table 1). Its mechanical behavior under dry conditions was studied in detail by *Klein et al.* [2001] and *Baud et al.* [2004] and more recently in water-saturated conditions by *Baud et al.* [2006].

2.2. Experimental Methodology

[10] The Diemelstadt sandstone samples were deformed in the Stony Brook laboratory. The samples were jacketed with a thin copper foil (0.05 mm thick) and then with polyolefine tubing before being placed in the pressure vessel. They were deformed at room temperature (air conditioned to 20°C) in the conventional triaxial configuration at confining pressures P_c ranging from 20 to 175 MPa, at a servo-controlled axial displacement rate of 0.5 μm/s. After accounting for the elastic deformation of the loading system and normalizing the sample displacement by the nominal length, this fixed displacement rate corresponds to a nominal axial strain rate of 1.3×10^{-5} s^{-1}. Displacement was measured outside the pressure vessel with a displacement transducer (DCDT) mounted between the moving piston and the fixed upper platen with an uncertainty of 10 μm in the measurement. The axial load was measured using an external load cell with an accuracy of 1 kN.

Table 1. Petrophysical Description of Sandstones With Discrete Compaction Band Failure Mode

Sandstone	Porosity, %	Grain Diameter, mm	Composition	Reference
Diemelstadt	24.3	0.16	Quartz: 68%, feldspar: 26%, oxides: 4%, micas: 2%	*Klein* [2002]; *Baud et al.* [2004]
Bleurswiller	25.2	0.224	Quartz: 50%, feldspar: 30%, oxide and mica: 20%	*Fortin et al.* [2005]
Bentheim	22.8	0.21	Quartz: 95%, kaolinite: 3%, orthoclase: 2%	*Vos* [1990]; *Klein and Reuschlé* [2003]
Aztec	20	0.1 − 0.5	Quartz: 93%, feldspar: 5%, kaolinite: 2%	*Sternlof et al.* [2005]
Navajo	<20%. 20 − 25%	0.05 − 0.25, 0.3 − 0.8	Quartz, minor: microcline and chert	*Mollema and Antonellini* [1996]

[11] We tested samples under both wet and dry conditions to study the effect of water. Samples for wet experiments were saturated with deionized water and deformed at a fixed pore pressure of 10 MPa under fully drained conditions. The pore volume change was recorded by monitoring the piston displacement of the pore pressure generator with a DCDT, and the porosity change was calculated from the ratio of the pore volume change to the initial bulk volume of the sample with an uncertainty of ±0.1%.

[12] We conducted 7 dry triaxial experiments at P_c = 60–180 MPa and a hydrostatic experiment to complement the data set of *Klein and Reuschlé* [2004]. The samples were dried in vacuum for 2 days at 80°C before the experiment. Longitudinal and transverse strains were measured by two electric resistance strain gauges. To circumvent the problem of breakage of strain gauges from stress-induced pore collapse, a thin layer of fast cured epoxy was first applied to fill up the surface pores before jacketing the sample with copper foil. The strain gauges were then mounted in orthogonal directions on the copper jacket at the midsection of the nominally dried samples. The volumetric strain was calculated from the strain gauge data by summing the axial strain and twice the transverse strain.

[13] Acoustic emission (AE) activity during the experiments was recorded using a piezoelectric transducer (PZT-7, 5.0 mm diameter, 1 MHz longitudinal resonant frequency) mounted on the flat surface of a spacer attached to the jacketed sample. The AE signals were conditioned by a preamplifier (gain 40 dB, frequency response 1.5 kHz to 5 kHz). To distinguish events from electric noise, a discriminator was used to check to amplitude and oscillation characteristics of the incoming signal [see *Zhang et al.*, 1990b for details].

[14] We performed nine experiments on Bleurswiller sandstone samples at effective pressures ranging from 10 to 200 MPa (Table 4). These include one hydrostatic compaction experiment performed in the Stony Brook laboratory and eight triaxial compression experiments performed in the Institut de Physique du Globe de Strasbourg. The experimental setup for the latter facility was described by *Klein and Reuschlé* [2003]. Although the sample dimensions (40 mm length and 20 mm diameter) for the Strasbourg experiments were slightly bigger and AE activity was not monitored, both the sample preparation and experimental protocol were identical to those in Stony Brook.

[15] The failed samples were impregnated with epoxy and then sawed along a plane parallel to the axial direction to prepare petrographic thin sections. The spatial distribution of damage in the thin sections of two failed samples was characterized quantitatively using a petrographic microscope in reflected light. Selected thin sections were also sputter coated with 3 nm of gold and studied using a LEO

1550 scanning electron microscope (SEM). The SEM micrographs were acquired as backscattered electron images at a voltage of 15 kV.

2.3. Diemelstadt Sandstone: Mechanical Behavior of Saturated and Dry Samples

[16] In this paper we will adopt the convention that compressive stresses and compactive strains (i.e., shortening and porosity decrease) are positive and we will denote the maximum and minimum principal compressive stresses by σ_1 and σ_3, respectively. The pore pressure will be denoted by P_p, and the difference between the confining pressure ($P_c = \sigma_2 = \sigma_3$) and pore pressure will be referred to as the effective pressure P_{eff}. The effective mean stress and the differential stress are given by $(\sigma_1 + 2\sigma_3)/3 - P_p$ and $\sigma_1 - \sigma_3$, respectively.

[17] We deformed a total of 15 saturated samples at effective pressures ranging from 10 MPa to 165 MPa. The mechanical data are compiled in Table 2, and the differential stress-axial strain curves for selected experiments are presented in Figure 1a. The curve of sample D19 deformed at P_{eff} = 10 MPa is representative of the three samples deformed in the brittle regime at effective pressures ≤40 MPa. The sample strain hardened to attain a peak stress, beyond which it strain softened to approach a residual stress. At elevated pressures of ≥60 MPa, the stress-strain curve showed an overall strain hardening trend that was punctuated by small stress drops. As elaborated by *Baud et al.* [2004] and *Louis et al.* [2006], these stress drop events in Diemelstadt sandstone were accompanied by episodic surges in AE rate, corresponding to the p-type AE activity as defined by *Baud et al.* [2004]. A typical set of AE data is shown in Figure 1b. In Figure 1a we also include mechanical data for three samples (D7, D13 and D14) all deformed at an effective pressure of 150 MPa. It can be seen that the mechanical behavior was quite variable, possibly related to the degree of heterogeneity from the presence of bedding laminae.

[18] In Figure 1c we plot the effective mean stress as a function of porosity change for selected saturated samples. For reference the data for hydrostatic compression of a saturated sample are shown as the dashed curve. The inflection point in the hydrostat coincided with an upsurge of AE activity and marks the critical pressure P^* for the onset of grain crushing and pore collapse [*Zhang et al.*, 1990a]. The nonhydrostatic and hydrostatic loadings are coupled in a conventional triaxial compression experiment. If the axial stress increases by an increment $\Delta\sigma_1$ while the confining and pore pressures are maintained constant, then the effective mean stress P and differential stress Q would increase by the amounts $\Delta\sigma_1/3$ and $\Delta\sigma_1$, respectively. If porosity change is elastic then it is solely controlled by the
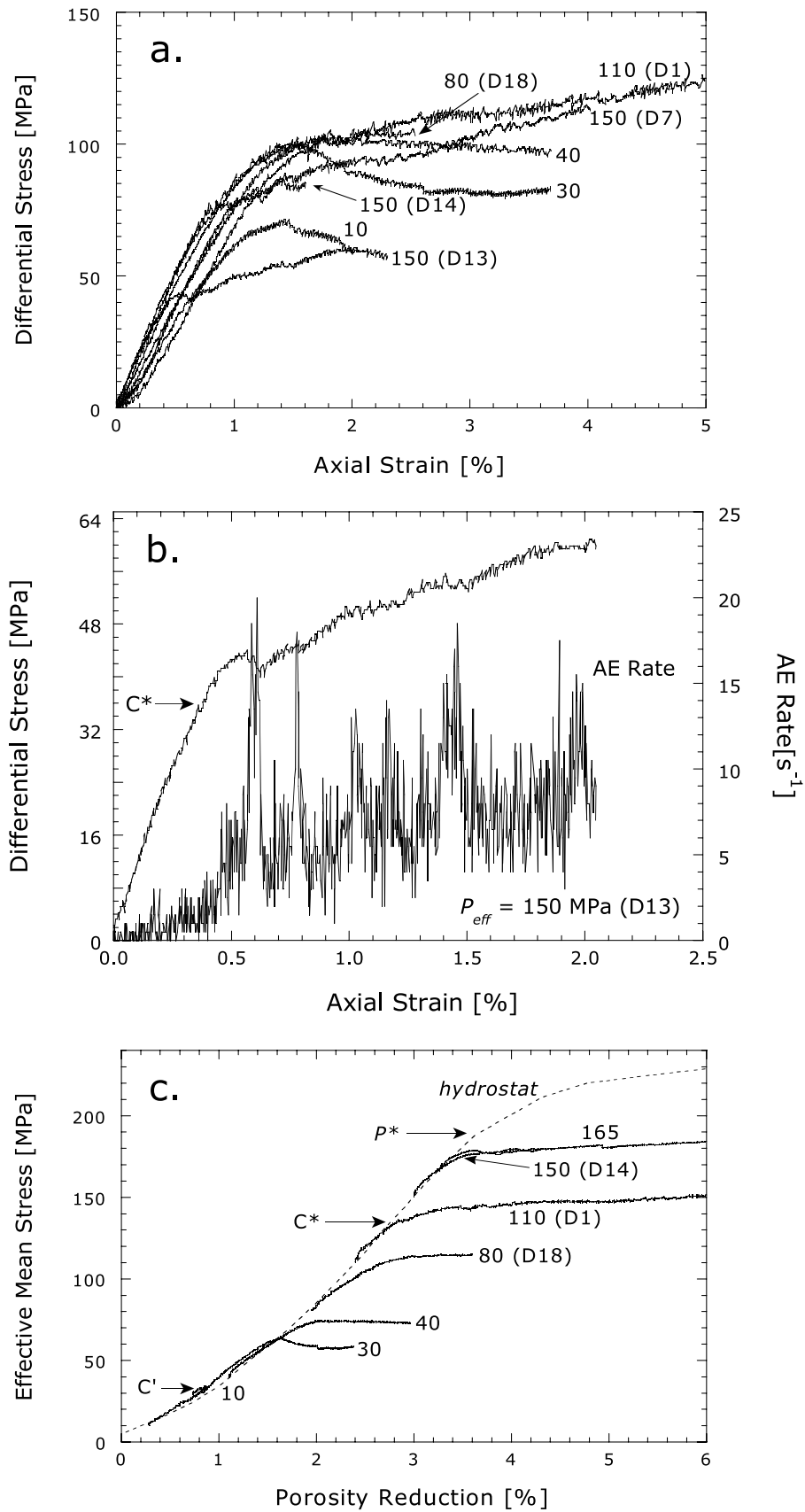
Figure 1

Table 2. Summary of Mechanical Data and Failure Mode for Wet Diemelstadt Sandstone[a]

Sample No.	Effective Pressure P_{eff}, MPa	Critical Yield Stress, MPa		Peak Stress, MPa		Failure Mode	Comments
		Differential Stress $\sigma_1 - \sigma_3$	Effective Mean Stress $(\sigma_1 + 2\sigma_3)/3 - P_p$	Differential Stress $\sigma_1 - \sigma_3$	Effective Mean Stress $(\sigma_1 + 2\sigma_3)/3 - P_p$		
			Dilatant C'				
D19	10	68	34	70	35	dilatant shear band	
			Compactant C*				
D15	30	78	56	101	64	shear band	
D10	40	83	68	103	75	high-angle shear band	inhomogeneous
D5	60	76	86	-	-	discrete CB + shear band	
D4	80	78	106	-	-	discrete compaction band	
D18	80	79	107	-	-	discrete compaction band	
D1	110	73	135	-	-	discrete compaction band	
D8	110	81	137	-	-	discrete compaction band	
D6	130	64	151	-	-	discrete compaction band	
D17	130	74	155	-	-	discrete compaction band	inhomogeneous
D7	150	65	173	-	-	discrete compaction band	
D13	150	36	161	-	-	discrete compaction band	
D14	150	65	172	-	-	discrete compaction band	inhomogeneous
D3	160	28	170	-	-	discrete compaction band	inhomogeneous
D11	165	37	178	-	-	discrete compaction band	
			P*				
D2	-	0	195	-	-	distributed cataclasis	
D33	-	0	195	-	-	distributed cataclasis	

[a]Samples where bedding was visible under 25× magnification or less are denoted as inhomogeneous.

hydrostatic stresses and independent of the differential stress, which would require the triaxial data (solid curves) in Figure 1c to coincide with the hydrostat (dashed curve). Deviations from the hydrostat can arise only if the porosity change in a triaxial compression experiment is inelastic, and therefore depends on not only the effective mean stress but also the deviatoric stresses. In all the experiments shown in Figure 1c the triaxial curve for a given effective pressure coincides with the hydrostat up to a critical stress state (marked as C' or C^*), beyond which there was an accelerated increase or decrease in porosity in comparison with the hydrostat. At stress levels beyond these critical stresses the deviatoric stress field provided a significant contribution to either the dilatational or compactive strain, corresponding to the onset and development of dilatancy and shear-enhanced compaction [*Wong et al.*, 1997]. Table 2 compiles the critical stresses C' for the onset of dilatancy and C^* for the onset of shear-enhanced compaction of the saturated samples. Dilatancy was observed only in the sample D19 deformed at effective pressure of 10 MPa. In the other 14 samples the inelastic deformation was compactant over a wide range of effective pressures between 30 to 165 MPa.

[19] The mechanical behavior of dry Diemelstadt sandstone at confining pressures ranging from room pressure to 35 MPa was comprehensively investigated by *Klein and*

Reuschlé [2004], in which dilatancy and brittle failure was observed (Table 3). To complement their data we conducted a hydrostatic compression experiment and eight triaxial experiments at confining pressures ranging from 60 MPa to 180 MPa (Figure 2). Shear-enhanced compaction was observed in all these samples, which was accompanied by episodic upsurges in AE rate corresponding to the p-type of AE activity defined by *Baud et al.* [2004].

2.4. Diemelstadt Sandstone: Strain Localization and Failure Modes

[20] The failure modes of *Klein and Reuschlé*'s [2004] and our samples are summarized in Tables 2 and 3, using the classification of deformation bands proposed recently by *Aydin et al.* [2006]. A deformation band is classified kinematically as a "shear" or "volumetric" deformation band according to whether the localized deformation is predominantly by shearing or volume change. The localized deformation in a shear band may involve a certain amount of volume increase or decrease, and accordingly these bands can be further distinguished to be either "compactive" or "dilatant" shear bands. If a volumetric deformation band was solely subjected to volume reduction or expansion, it is called a "compaction band" or "dilation band". It should be noted that the distinction between "shear" and "volu-

Figure 1. Representative mechanical data for triaxial compression experiments on saturated Diemelstadt sandstone. (a) Differential stress versus axial strain for experiments at the effective pressures indicated (in MPa) next to each curve. (b) Differential stress and acoustic emission (AE) rate as a function of axial strain in a triaxial experiment at an effective pressure of 150 MPa. The formation of a single discrete compaction band is associated with a small stress drop and a spike in the AE rate. This sample (D13) had approximately five bands developed. (c) Effective mean stress versus porosity reduction. For reference, the hydrostatic data are shown as dashed lines. The arrow indicates the critical pressure P^* for the onset of pore collapse. The mechanical behavior of saturated Diemelstadt is predominantly compactant.

Table 3. Summary of Mechanical Data and Failure Mode for Dry Diemelstadt Sandstone

Sample No.	Confining Pressure P_c, MPa	Critical Yield Stress, MPa		Peak Stress, MPa		Failure Mode	Reference
		Differential Stress $\sigma_1 - \sigma_3$	Mean Stress $(\sigma_1 + 2\sigma_3)/3 - P_p$	Differential Stress $\sigma_1 - \sigma_3$	Mean Stress $(\sigma_1 + 2\sigma_3)/3 - P_p$		
				Dilatant C'			
-	5	24	13	62	27	shear band	*Klein and Reuschlé* [2004]
-	10	36	22	77	39	shear band	*Klein and Reuschlé* [2004]
-	15	50	32	89	50	shear band	*Klein and Reuschlé* [2004]
-	20	53	38	98	59	shear band	*Klein and Reuschlé* [2004]
-	25	62	46	108	69	shear band	*Klein and Reuschlé* [2004]
-	30	78	56	121	80	shear band	*Klein and Reuschlé* [2004]
				Compactant C*			
D31	60	138	106	143	108	discrete CB + shear band	this study
D34	80	139	127	-	-	discrete compaction band	this study
D39	90	131	134	-	-	discrete compaction band	this study
D38	110	121	150	-	-	discrete compaction band	this study
D35	130	105	165	-	-	discrete compaction band	this study
D37	150	105	185	-	-	discrete compaction band	this study
D36	180	81	207	-	-	discrete compaction band	this study
				P*			
D30	-	0	260	-	-	distributed cataclasis	this study

metric'' deformation bands can be imprecise in some situations. It is suggested by one of the reviewers [J. W. Rudnicki, personal communication, 2007] that a better classification would be in terms of shear and normal deformation relative to the plane of the band. Moreover, using the terminology introduced by *Baud et al.* [2004] on the basis of their data for five sandstones with porosities ranging from 13% to 24%, a localized structure that has a thickness of only a few (say ≤3) grains is referred to as a ''discrete band'', whereas thicker structures are called ''diffuse band''.

[21] In Figure 3 we present a series of micrographs of the failed samples to illustrate the progressive transition in failure mode with increasing effective pressure related to dilatant and compactant failure in Diemelstadt sandstone.

Although we only show thin sections for the saturated samples, it should be emphasized that the failure mode in the dry samples and its transition with increasing confining pressure are qualitatively similar. Shear bands were observed in the three samples deformed at effective pressures ≤40 MPa. Many of these shear bands seem to have initiated from the sample corners, and with increasing strain propagated across the sample at an angle of 32° with respect to σ_1 in dilatant sample D19 (Figure 3a) and up to 65° in the sampled D10 (Figure 3c) deformed at effective pressures of 10 MPa and 40 MPa, respectively. While two conjugate bands had developed in the dilatant sample D19, a mosaic of several intersecting shear bands were observed in the samples D15 and D10 that underwent shear-enhanced compaction (Figures 3b and 3c).
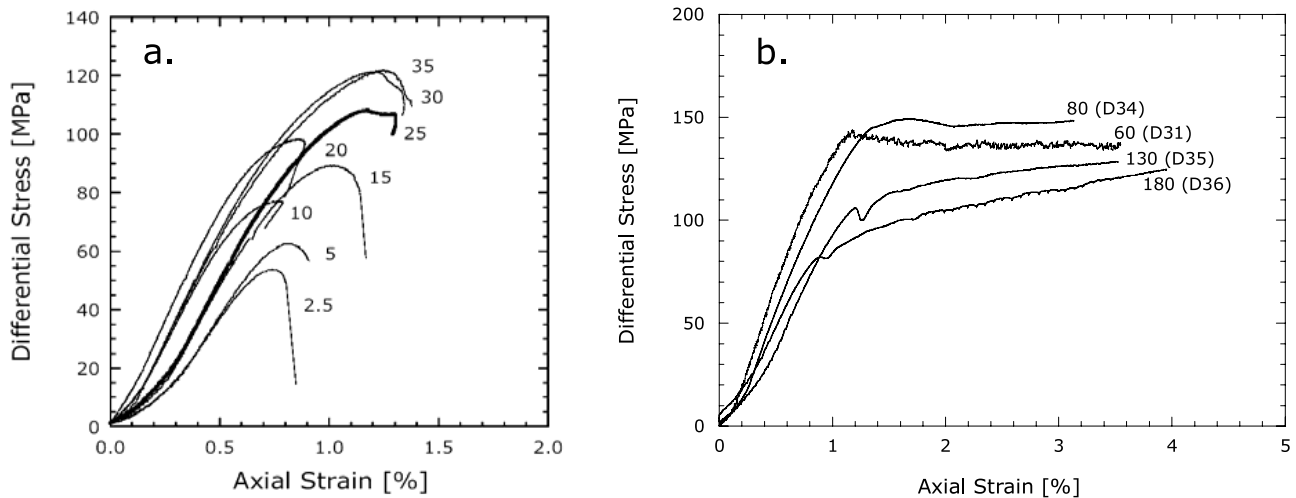

Figure 2. Representative mechanical data for selected triaxial compression experiments on dry Diemelstadt sandstone. Differential stress versus axial strain, at effective pressures indicated (in MPa) next to each curve, for (a) samples deformed in the dilatant brittle regime by *Klein and Reuschlé* [2004] and (b) selected samples with compactant failure.
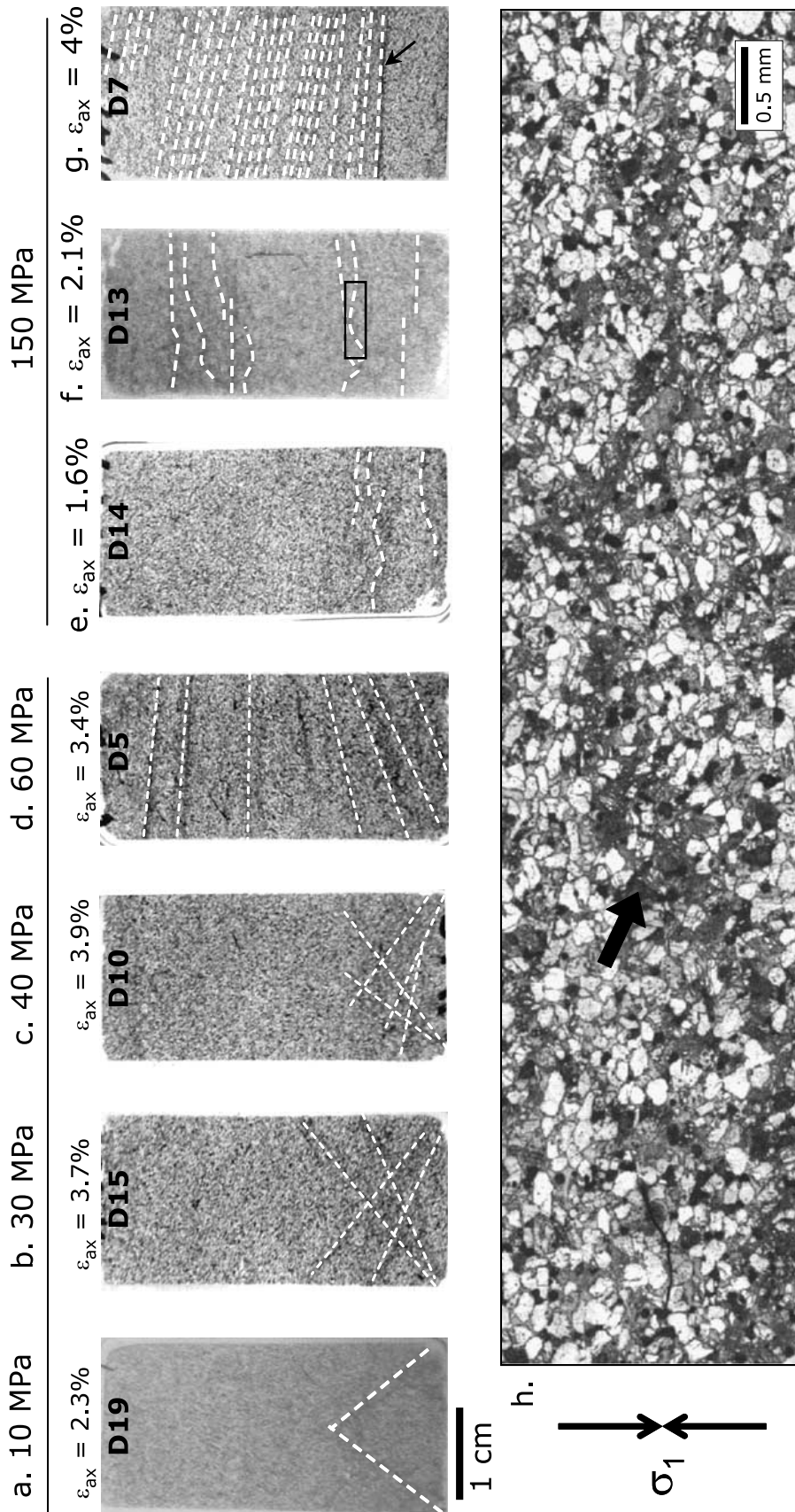
Figure 3. Transmission optical micrographs of deformed wet Diemelstadt sandstone samples. The effective pressure and the level of axial strain are indicated next to the thin sections. The width of each thin section is ~18 mm. Principal stress σ_1 was along the axial direction. Brittle failure in the Diemelstadt sandstone occurs at effective pressures of 10–60 MPa as (a) dilatant conjugate shear-bands, (b) compactant conjugate shear-bands, (c) diffuse conjugate shear-bands, and (d) mixed failure modes of high-angle shear-bands and compaction bands. At higher pressure (>60 MPa), discrete compaction bands are the dominant failure mode. The development of an array of discrete compaction bands at 150 MPa effective pressure can be traced with increasing axial strain: (e) 1.6%, (f) 2.1%, and (g) 4%.The black arrow in Figure 3g points to a layer of oxides separating coarser material below from finer material above. (h) Mosaic showing a discrete compaction band propagating across the sample in the area delimited by a rectangle in sample D13 (f). Significant comminution makes the band appear dark.
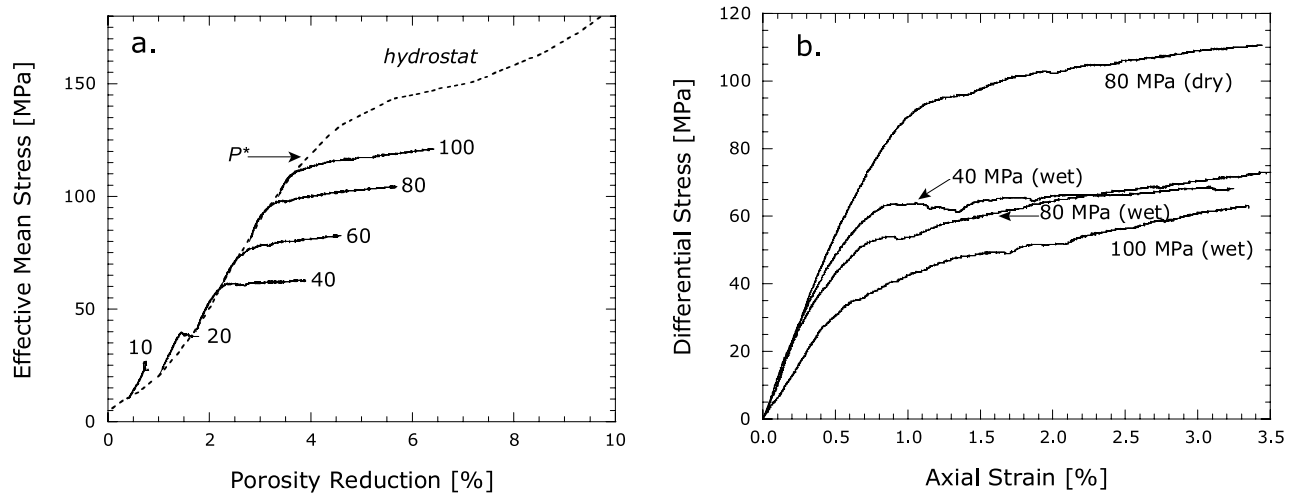
Figure 4. Representative mechanical data for triaxial compression experiments on Bleurswiller sandstone. (a) Effective mean stress versus porosity reduction for experiments on saturated samples at effective pressures indicated (in MPa) next to each curve. For reference, the hydrostatic data are shown as dashed lines. The arrow points to the critical pressure P^* for the onset of pore collapse. (b) Differential stress versus axial strain for three representative experiments on saturated samples and for a single dry experiment performed at 80 MPa confining pressure.

[22] With increasing effective pressure a transition of failure mode from shear bands to discrete compaction bands was observed. The geometric complexity associated with this transition is manifested by the hybrid development of both high-angle shear bands and discrete compaction bands in sample D5 deformed at effective pressure of 60 MPa (Figure 3d). Discrete compaction bands are representative of the failure mode observed throughout the ductile regime at pressures ≥60 MPa. Distributed cataclastic flow was not observed in any of our triaxial experiments. Multiple experiments at the same effective pressure 150 MPa captured the cumulative development of discrete compaction bands with increasing strain. The samples D7, D13, and D14 were deformed to ultimate axial strains of 1.6% to 4.0% (Figures 3e–3g). Following the onset of shear-enhanced compaction, discrete compaction bands initiated in short segments near the ends of sample. With increasing strain the discrete bands cut through the cross-section of the sample and clustered to form subparallel arrays that spread toward the center of the sample. We observed that the number of discrete bands, episodic stress drops and AE upsurges are correlated in a manner similar to that in the Bentheim sandstone [Vajdova et al., 2004], which has been attributed to discrete instability events each of which can be identified with the unstable propagation of a discrete compaction band normal to σ_1. The initiation and propagation of a discrete compaction band is accomplished by intense grain crushing and pore collapse localized (Figure 3h) within a tabular zone with lateral thickness of 2–3 grains (or ~450 μm). Assuming the lateral strain after C^* is negligible, the porosity reduction in a single band may be estimated by normalizing the inelastic axial shortening by the total average thickness of the bands per number of bands. For sample D13 the inelastic axial strain and equivalently the porosity reduction was found by Louis et al. [2006] to be $\Delta\phi \sim 13.8\%$. Vajdova et al. [2004] performed a similar calculation for

Bentheim sandstone and obtained $\Delta\phi \sim 14\%$. Baud et al. [2004] estimated the porosity reduction in Bentheim indirectly from the number of AE surges and obtained a comparable estimate of $\Delta\phi \sim 15\%$.

[23] Bedding is observed to influence compaction band orientation such that the structures will form and propagate subparallel to the bedding plane with an orientation of 75–90° relative to maximum compressive stress σ_1 and at the boundary of the low-porosity laminae. A layer of oxides (which appear black in thin section) separates finer grained material in the upper part of the section from the coarser material at the bottom in Figure 3g. Samples in which bedding was visible in the thin section at low magnification (25×) are denoted as "inhomogeneous" in Table 1.

[24] Damage in macroscopically homogeneous samples D33 and D32 which were hydrostatically deformed to just beyond the grain crushing pressure P^* before being unloaded were characterized by pore collapse and Hertzian fractures [Menéndez et al., 1996] radiating from grain contacts.

2.5. Bleurswiller Sandstone: Mechanical Data of Saturated and Dry Samples

[25] In Figure 4a we present data for the effective mean stress as a function of porosity reduction in selected triaxial compression experiments on saturated samples. For reference the hydrostat is included as the dashed curve, with the critical pressure P^* for onset of grain crushing and pore collapse marked. At 10 MPa effective pressure the sample failed by dilatant brittle failure. Shear-enhanced compaction was observed in all saturated samples at effective pressures of 20 MPa and above. The mechanical data are summarized in Table 4. Our data for the brittle strength and compactive yield stress C^* of saturated samples are comparable to those obtained by Fortin et al. [2005].

Table 4. Critical Stresses and Failure Mode of Saturated and Dry Bleurswiller Sandstone

Sample No.	Effective Pressure P_{eff}, MPa	Critical Yield Stress, MPa		Peak Stress, MPa		Failure Mode
		Differential Stress $\sigma_1 - \sigma_3$	Effective Mean Stress $(\sigma_1 + 2\sigma_3)/3 - P_p$	Differential Stress $\sigma_1 - \sigma_3$	Effective Mean Stress $(\sigma_1 + 2\sigma_3)/3 - P_p$	
			Dry			
BL2	80	81	107	-	-	discrete compaction band
			Wet			
BL15	10	-	-	49.5	26.6	dilatant shear band
BL13	20	54	38	-	-	discrete compaction band + shear band
BL3	40	53	58	-	-	discrete compaction band + shear band
BL7	50	45	65	-	-	discrete compaction band + shear band
BL4	60	40	73	-	-	discrete compaction band
BL1	80	29	90	-	-	discrete compaction band
BL5	100	17	105	-	-	discrete compaction band
			P* (wet)			
BL19	-	0	118	-	-	distributed cataclasis

[26] In Figure 4b we present the data for the differential stress as a function of axial strain in three wet and one dry experiments. In these samples, the development of shear-enhanced compaction was accompanied by an overall strain hardening trend punctuated by several moderate stress drops. Data at the same effective pressure of 80 MPa for a saturated and a dry sample indicate significant weakening of the Bleurswiller sandstone in the presence of water. It should be noted that although *Fortin et al.* [2005] did not report any triaxial compression tests on dry samples, their hydrostatic compaction data indicate modest water weakening, manifested by *P** values of 180 MPa and 135 MPa in the dry and saturated samples, respectively [*Fortin et al.*, 2007].

[27] Since we have not conducted systematic microstructural study on Bleurswiller sandstone, we rely here on the observations of *Fortin et al.* [2005] which were primarily on the basis of exterior appearance of the failed samples. They reported discrete compaction band formation in saturated samples that failed at effective pressures of 40, 60, 80 and 100 MPa (reported by *Fortin et al.* [2005] as experiments conducted at confining pressures of 50, 70, 90, and 100 MPa). While shear bands seem to be absent in the samples failed at 80 and 100 MPa, a hybrid failure mode was observed at effective pressures of 40 and 60 MPa, involving both discrete compaction bands and conjugate shear bands. Preliminary observations on low-strain samples suggest localization initiates from stress heterogeneities caused by pores and weak grains and present in the Bleurswiller.

3. Discussion

3.1. Yield Stresses for Compaction Band Formation: Effect of Mineralogy and Water

[28] *Zhang et al.* [1990a] proposed a Hertzian fracture model which predicts that the grain crushing pressure *P** in a siliciclastic rock would scale with $(D\phi)^{-1.5}$ (where *D* and ϕ denote the grain size and porosity, respectively). Since Diemelstadt, Bleurswiller, and Bentheim sandstones have comparable grain size and porosity, one expects from this model that the onset of grain crushing and pore collapse in these sandstones would involve effective pressures on the

same order of magnitude. However, it should be noted that *Wong et al.* [1997] also show that other factors (including mineralogy and bedding) can appreciably influence the grain crushing pressure and critical stresses, such that at the same porosity and grain size the yield stresses may deviate by as much as a factor of 2 from the trend predicted by the Hertzian fracture model.

[29] Such variability is observed in Figure 5, which shows the porosity reduction and AE activity in our saturated samples of these three sandstones under hydrostatic loading. It can be seen that Bentheim sandstone (Figure 5c) stands out in two respects. First, its grain crushing pressure has a magnitude more than twice the other two sandstones. Second, as soon as the critical pressure *P** was attained, its porosity reduction occurred almost as a runaway instability, with the applied pressure basically unchanged. The somewhat anomalous behavior in Bentheim sandstone is possibly related to its relatively homogeneous mineralogy (with 95% quartz). In contrast, the significantly lower critical pressures in Bleurswiller (Figure 5a) and Diemelstadt (Figure 5b) sandstones may be related to the relative abundance of weaker secondary phases, such as feldspar and mica (Table 1). The more diverse mineralogy would likely result in a stronger heterogeneity in the local stress field and fracture toughness, and accordingly incremental increases in applied pressure are required to sustain the progressive development of grain crushing and pore collapse.

[30] In Figure 6a we summarize the brittle strength and the critical stress *C** for Bleurswiller sandstone. The data of *Fortin et al.* [2005, 2006, 2007] are included as the grey symbols. Figure 6b compiles our data for Diemelstadt sandstone, and Figure 6c shows the data for Bentheim sandstone of *Baud et al.* [2004, 2006]. As typical of the brittle-ductile transition in porous siliciclastic rocks [*Wong et al.*, 1997], brittle failure in these porous sandstones is characterized by a Coulomb-type strength envelope, while the onset of compactive yield is characterized by an approximately elliptic cap in the space of effective mean stress and differential stress.

[31] *Wong et al.* [1997] proposed that the compactive yield stress *C** would scale with the porosity and grain size
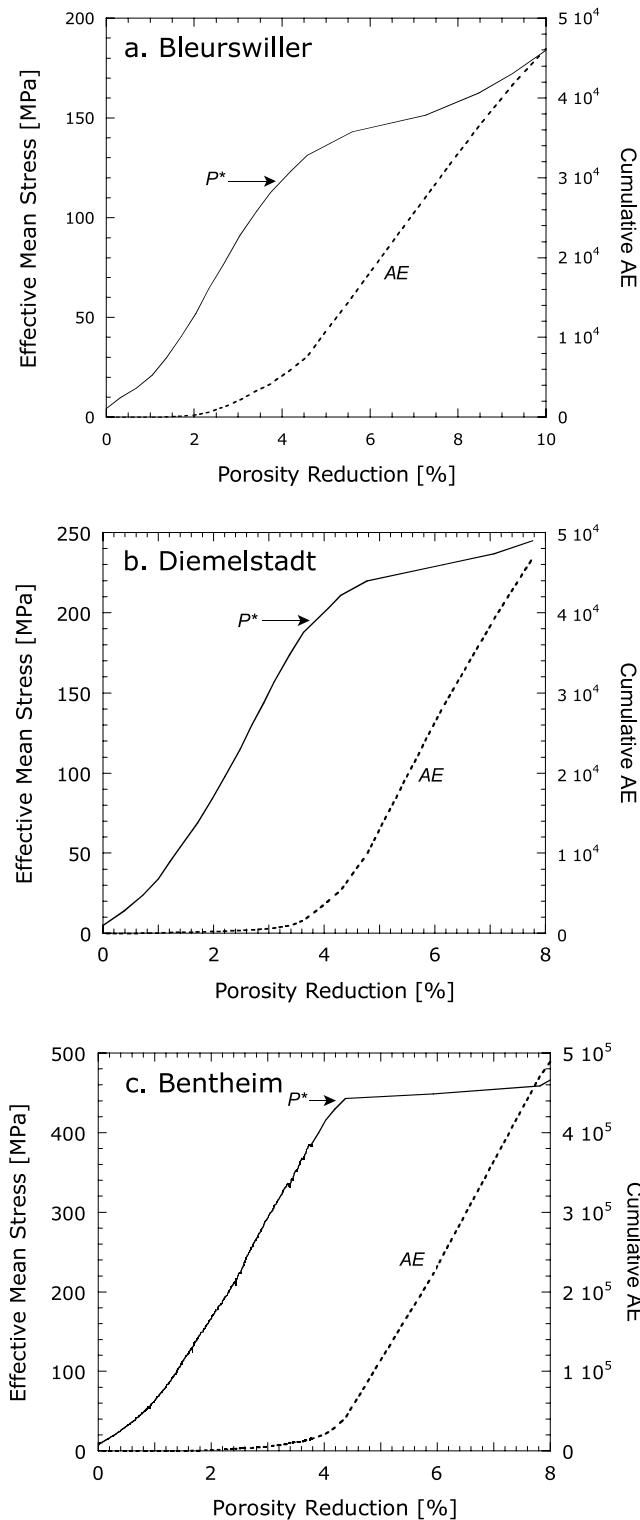
Figure 5. Effective pressure and cumulative count of AE as functions of porosity reduction in hydrostatic experiments on (a) Bleurswiller, (b) Diemelstadt, and (c) Bentheim sandstones. The arrows indicate the critical pressures $P*$ for the onset of pore collapse.
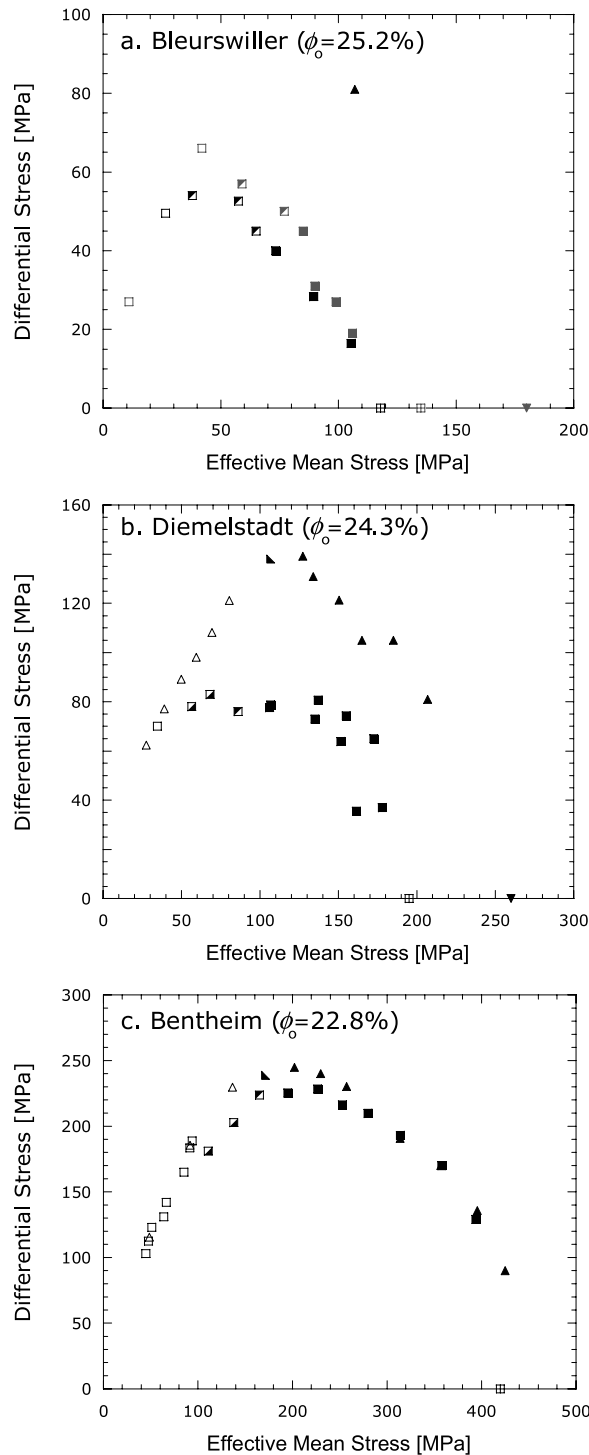
in a manner similar to the grain crushing pressure $P*$. Indeed the yield envelopes in Figure 6 show that both the compactive yield stresses and grain crushing pressure in Bentheim sandstone are significantly higher than the other two sandstones. Bentheim sandstone is also anomalous in that its yield stress seems to be almost insensitive to the presence of water (Figure 6c). In comparison, the compactive yield stresses in saturated samples of Diemelstadt sandstone were lower by 20–40% than those in the dry samples deformed under comparable pressure conditions (Figure 6b). The single triaxial compression experiment we conducted on a dry Bleurswiller sandstone sample suggests an even stronger water-weakening effect (Figure 6a). The reduction in strength observed in Bleurswiller and Diemelstadt sandstones falls in the range of 20–70% reported by *Baud et al.* [2000] in four sandstones with porosities ranging from 11% to 35%. They also observed an overall trend for the water-weakening effect to be more pronounced in feldspar-rich sandstone, which would imply significantly lesser water weakening in Bentheim sandstone that is primarily made up of quartz. The data synthesized here demonstrate the three sandstones develop discrete compaction bands over a broad range of effective pressures and the stress level involved in band formation varies by a factor of 5 or so among these sandstones of similar porosity and grain size. The presence of weak secondary phases and water can significantly lower the stresses necessary for this type of compaction localization.

[32] Figure 7 compares the stresses for compaction band formation in the laboratory samples with field data on the Aztec sandstone [*Sternlof et al.*, 2005]. In the two quartz sandstones of Bentheim and Aztec, the stresses vary by an order of magnitude. Although mineralogy influences stress magnitude, it appears not to be a primary factor associated with the compaction band failure mode.

3.2. Geometric Attributes of Compaction Bands and Scaling Relation

[33] The geometric attributes of discrete compaction bands have been systematically characterized in laboratory deformed samples. Fairly extensive data on the thickness, tortuosity, and spacing are available from quantitative microstructural observations [*Baud et al.*, 2004; *Vajdova et al.*, 2004; this study], X-ray CT imaging [*Louis et al.*, 2006] and AE locations [*Fortin et al.*, 2005]. A common observation is that the initiation and propagation of compaction bands seem to be controlled by grain-scale heterogeneities. The discrete bands made up of intensely comminuted grains typically span laterally over ~2–3 grains, with thicknesses <1 mm.

[34] While the geometry of compaction bands observed in the field is qualitatively similar, their dimensions are appreciably larger, with the implication that they reflect spatial heterogeneities with dimensions greater than the grain size. *Sternlof et al.* [2005] observed band thickness on the order of 1–10 mm in the Valley of Fire and noted the band thickness and length seemed to be positively correlated. In their seminal work *Mollema and Antonellini* [1996] differentiated between two types of discrete compaction bands in the porous Navajo sandstone (20–25 % porosity): thick and crooked. Thick bands were 0.5 to 1.5 cm in lateral thickness with trace lengths around 5–10 meters, and crooked bands

had a thickness of 0.1 to 0.5 cm and trace lengths up to 2 meters. *Hill* [1989] observed compaction bands with an average thickness of 0.5 mm and length of 1.25 m in the Valley of Fire at a site 2 km west of that of *Sternlof et al.* [2005].

[35] We compile in Table 5 and Figure 8 field and laboratory data on compaction band thickness and length. Since the compaction bands cut through the laboratory sample, the diameter provides a lower bound on the band length. We will denote the maximum thickness and length by $2t_{max}$ and $2L$, respectively (Figure 9a). It can be seen from Table 5 that the aspect ratio t_{max}/L is on the orders of $10^{-3}-10^{-4}$ and 10^{-2} for the field and laboratory data, respectively.

[36] *Sternlof et al.* [2005] noted that measurements of lateral thickness along a compaction band provide a proxy for the variation of inelastic closure. With reference to Figure 9a, if we denote the inelastic normal strain within the compaction band by ε^p, then the normal displacement discontinuity Δw due to inelastic closure is related to the band thickness t by $\Delta w(x) = 2t(x)\varepsilon^p/(1 - \varepsilon^p) \approx 2t(x)\varepsilon^p$. Hence if the compactant strain ε^p localized within the compaction band is relatively uniform, then the inelastic closure Δw is directly proportional to band thickness t. Accordingly a correlation between band length L and maximum thickness t_{max} would imply a similar correlation between band length L and maximum inelastic shortening Δw_{max}.

[37] It is of interest to note that a positive correlation between band length and maximum slip (or tangential displacement discontinuity) has been widely observed in shear localization structures in porous sandstone formations. As reviewed by *Kim and Sanderson* [2005], extensive field data have been accumulated on the scaling between deformation band length L and maximum slip δ_{max}, and the field data indicate a scaling relation of the form $\delta_{max} = cL^n$ with a typical value of the exponent $n \sim 1$ [e.g., *Cowie and Scholz*, 1992]. A linear scaling relation $\delta_{max} \propto L$ can be interpreted as due to a uniform shear stress drop associated with a self-similar propagation of an elliptical slip profile. However, it should be noted that there are settings for which higher and lower exponent values have been determined. In particular, *Fossen and Hesthammer* [1997] reported a scaling relation with $n \sim 0.54$ for 31 isolated deformation bands in Jurassic sandstone in Goblin Valley in southeastern Utah. Except for the longest one which has a length of ~ 100 m, these deformation bands are relatively short with lengths ranging between 0.15 and 20 m.

[38] The deformation band data motivate us to explore whether a similar scaling relation between band length and normal displacement discontinuity applies to compaction bands. The field and laboratory data compiled in Table 5 are plotted in Figure 8 on logarithmic scales. The

Figure 6. Critical stresses and failure modes in P–Q space for (a) Bleurswiller, (b) Diemelstadt, and (c) Bentheim sandstones. Wet data are represented by squares, and dry data are represented by triangles. Dilatant and compactant samples are indicated by open and closed symbols, respectively. The grey symbols in Figure 6a are data from *Fortin et al.* [2005, 2006, 2007]. Data on Bentheim sandstone are from *Baud et al.* [2004, 2006].
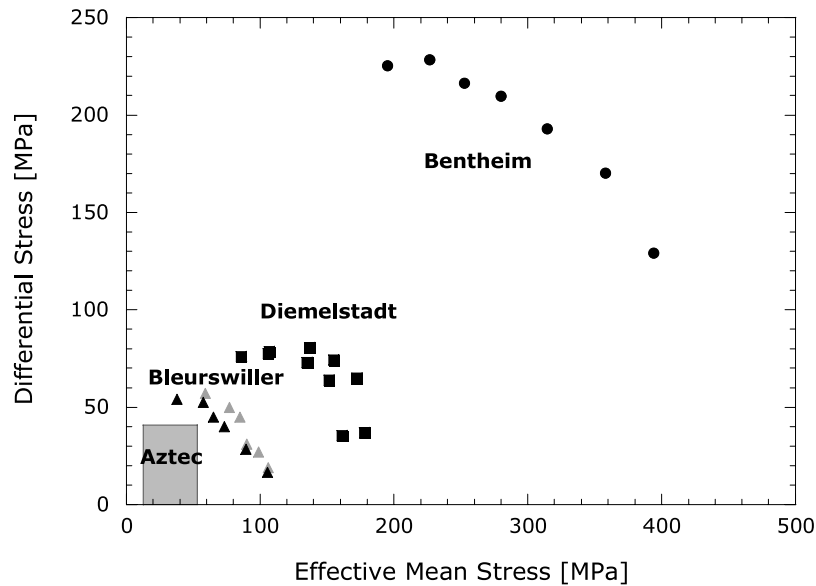
Figure 7. Yield stresses at the onset of shear-enhanced compaction for saturated samples developing discrete compaction bands. Bentheim (circles) [*Baud et al.*, 2004, 2006], Diemelstadt (squares), and Bleurswiller (triangles) sandstones have been studied in the laboratory. The grey symbols are data on Bleurswiller sandstone from *Fortin et al.* [2005, 2006]. The shaded rectangle is the inferred paleostress for the Aztec sandstone [*Sternlof et al.*, 2005].

data extending over four orders of magnitude can be fitted with a power law

$$t_{\max} = cL^n \qquad (1)$$

with an exponent $n = 0.41$ determined by linear regression. If we restrict the linear regression to only the field data, then a somewhat larger exponent $n = 0.50$ is obtained.

[39] To interpret the compaction band data, we will adopt a theoretical model recently developed by *Rudnicki* [2007], that predicts a scaling relation with an exponent $n = 0.5$. He noted that the Valley of Fire data of *Sternlof et al.* [2005] for thickness $t(x)$ tend to deviate from an overall elliptical trend as predicted for an anticrack model [*Fletcher and Pollard*, 1981]. Since the data seem to trace a relatively flat plateau
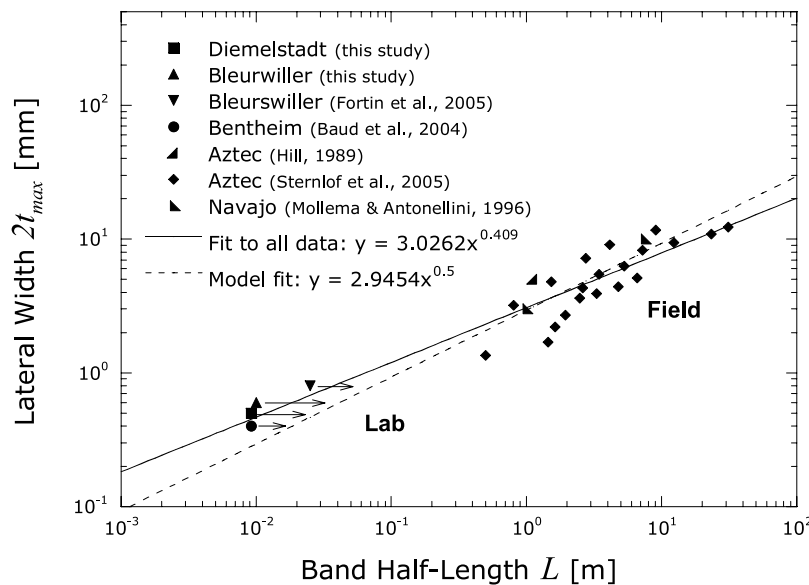

Figure 8. Compilation of laboratory and field observations on the thickness and half-length of a discrete compaction band. The solid line is a best fit to all the data and suggests a quadratic scaling relationship between the dimensions. The dashed line is the prediction by *Rudnicki* [2007] anti-crack/dislocation model and very closely approximates the field data. Since the compaction bands in laboratory experiments are constrained by the width of the sample, the model implies that their full width would lie on the dashed line.
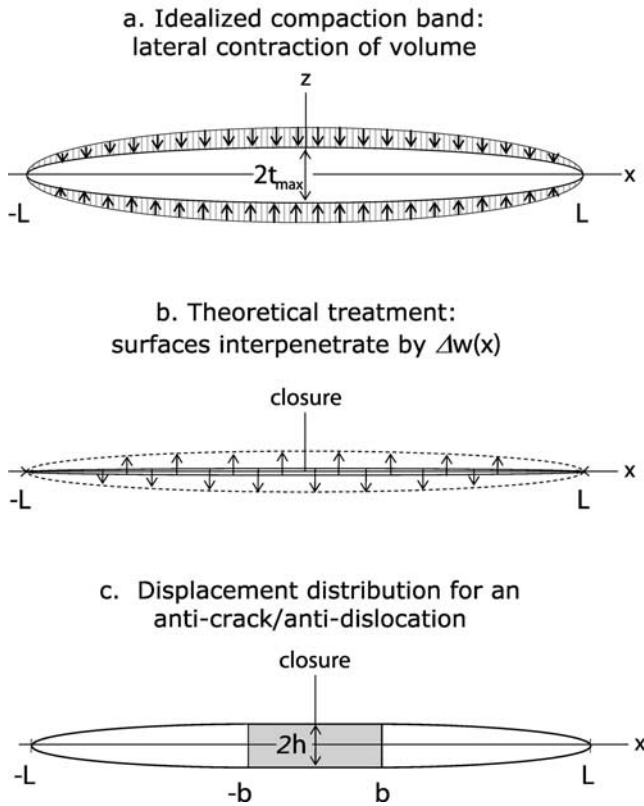
Figure 9. (a) Cross-section of an idealized compaction band as an elongate structure (white ellipse). The grey area is the predeformation volume of the band. Following axisymmetric compression, the volume shrinks to a band with thickness $2t$ and length $2L$ (compiled in Table 5). The resulting inelastic plastic strain is ε_p and inelastic shortening is Δw. (b) Theoretical treatment of the idealized compaction band as a closing-mode displacement discontinuity where the material surfaces interpenetrate to the dashed line by $\Delta w(x)$. Displacements are shown as opening for clarity but correspond to interpenetration (compaction) in the model. Actual interpenetration does not occur. (c) Displacement of the material surface in the band shown in Figure 9b follows a distribution of a combined anti-crack/anti-dislocation [Rudnicki, 2007]. A uniform compactive displacement of $2h$ is specified for $-b \leq x \leq b$, and a uniform closure traction, equal to the difference between the far field compressive stress and the resistive stress, is specified for $|b| > x \leq |L|$.

near the middle ($x = 0$), *Rudnicki* [2007] proposed a combined anti-crack/anti-dislocation model. In an anticrack model, the compaction band is considered to be an elongate structure with negligible initial thickness, and the normal

displacement discontinuity Δw due to inelastic closure corresponds to an interpenetration of the contacting band surfaces (Figure 9b). Assuming a uniform normal traction within the band, the inelastic closure Δw would have an elliptical profile and incorporating an antidislocation would modify the profile by flattening it near the middle (Figure 9c).

[40] Since the anticrack/antidislocation model here involves compressive normal stress and inelastic closure, this configuration is identical to that for a combined crack/dislocation that has been investigated in linear elastic fracture mechanics [*Tada et al.*, 1973], but with the signs of the stress and displacement reversed. The compaction band has total length $2L$ with a uniform inelastic closure $2h$ prescribed near the middle for $-b \leq x \leq b$ and a uniform compressive traction $\Delta\sigma$ applied on the region outside for $b \leq |x| \leq L$ (Figure 9c). Hence the maximum inelastic closure is $\Delta w_{max} = 2h$. The traction $\Delta\sigma$ is equal to the difference between the far-field compressive stress σ_{zz}^{∞} and the resistive stress in the band σ_{zz}^{r}. There is the possibility that the resistive stress in the field may be different from that in the laboratory, but this is and issues difficult to constrain with existing data. Following *Rudnicki and Sternlof* [2005] we will assume here $\Delta\sigma \approx \sigma_{zz}^{\infty}$. The magnitude of this traction should be chosen to eliminate the singularity in stress induced by the antidislocation at $x = \pm b$, or equivalently, to ensure that the tangent to the profile of crack surface displacements is continuous. The traction is given by *Rudnicki* [2007]

$$\Delta\sigma = \sigma_{zz}^{\infty} = \left(\frac{Eh}{2(1-\nu^2)L}\right)\left\{\frac{1}{\left[E_1(k) - (b/L)^2 E_2(k)\right]}\right\} \quad (2)$$

where $k = \sqrt{1 - (b/L)^2}$ and E_1 and E_2 are the complete elliptic integrals of the first and second kinds, respectively. The Young's modulus and Poisson ratio are denoted by E and ν, respectively. The stress field at the ends of the compaction band is singular, with a stress intensity factor given by

$$K = \sqrt{\frac{\pi}{L-b}}\frac{Eh}{(1-\nu^2)}\left(\frac{k\sqrt{1-b/L}}{E_1(k) - (1-k^2)E_2(k)}\right) \quad (3a)$$

The bracketed term above equals unity in the limit as $b/L \to 0$ ($k \to 1$). However, *Rudnicki* [2007] also demonstrated that the bracketed term has a value close to 1 not only for $b/L \to 0$, where it is exact, but over most of the range of b/L.

Table 5. Geometric Attributes of Discrete Compaction Bands and Associated Stress States

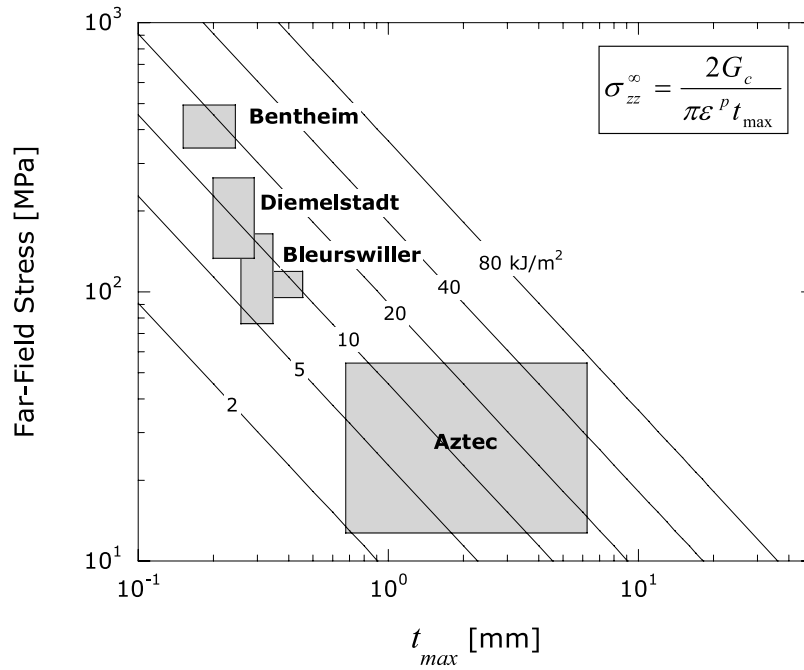| Sandstone	t_{max}, mm	L, m	σ_{zz}^{∞}, MPa	Reference
Bentheim	0.2	>0.0092	339−496	*Baud et al.* [2004, 2006]
Diemelstadt	0.25	>0.0092	136−261	this study
Bleurswiller	0.3	>0.01	74−161	this study
	0.4	>0.025	97−119	*Fortin et al.* [2005]
Aztec	2.5	1.1	-	*Hill* [1989]
	0.675−6.15	0.5−31	13−54[a]	*Sternlof et al.* [2005]
Navajo	0.5−2.5, 2.5−7.5	≤2, 5−10	-	*Mollema and Antonellini* [1996]

[a]Pore pressure was not considered.

Figure 10. An extension of the anti-crack/anti-dislocation model predicts that the far-field stress would scale with the band half-thickness t (as well as h). The solid black lines are the stresses predicted by equation (7) assuming a plastic strain of 0.14 for a range of energy release rates. The grey boxes are laboratory and field data (listed in Table 5).

Consequently the stress intensity factor for the anticrack/antidislocation model can be approximated by

$$K = \frac{\sqrt{\pi}}{L} \frac{Eh}{2(1 - \nu^2)} \qquad (3b)$$

and the strain energy release rate by

$$G = \frac{(1 - \nu^2)}{E} K^2 = \frac{\pi E h^2}{4(1 - \nu^2) L} \qquad (4a)$$

as long as b/L is not too large ($b/L < 0.3$). The condition for propagation of the compaction band is for the stress intensity factor or strain energy release rate to attain a critical value:

$$G = G_c = \frac{\pi E h^2}{4(1 - \nu^2) L} \qquad (4b)$$

where G_c denotes the critical strain energy release rate or compaction energy [*Vajdova and Wong*, 2003; *Rudnicki and Sternlof*, 2005; *Tembe et al.*, 2006].

[41] According to (4b) the maximum inelastic closure h and compaction band length L are related by

$$\frac{h}{2\sqrt{L}} = \sqrt{\frac{G_c(1 - \nu^2)}{\pi E}} \qquad (5a)$$

As discussed above, if the inelastic strain localized inside the compaction band is ε^p, then the maximum inelastic

closure is $\Delta w_{max} = 2h = 2\varepsilon^p t_{max}$ and therefore the maximum band thickness is given by

$$\frac{t_{max}}{\sqrt{L}} = \frac{2}{\varepsilon^p} \sqrt{\frac{G_c(1 - \nu^2)}{\pi E}} \qquad (5b)$$

If the compaction energy, localized compaction and elastic moduli have comparable magnitudes in the laboratory samples and field settings, then this model of *Rudnicki* [2007] predicts that the maximum thickness of a compaction band scales as the square root of the band length L, which would correspond to the scaling relation (1) with an exponent $n = 0.5$. With reference to (5b), the dashed line in Figure 8 corresponds to a compaction energy $G_c \approx 1$ kj/m^2 if we assume $\varepsilon^p = 0.1$, $E = 30$ GPa and $\nu = 0.2$. In contrast, an anticrack model (without embedding the antidislocation) would predict a linear relation with $n = 1$.

3.3. Spatial Heterogeneity and Stress State for Compaction Band Formation

[42] Implicit in the study of *Rudnicki*'s [2007] anticrack/antidislocation model is the assumption that the propagation behavior and geometric attributes of compaction bands are controlled by the spatial scale of heterogeneity that can be quite different in laboratory and field settings. A measure of such spatial heterogeneity is given by the band thickness, which is comparable to the grain scale in a relatively homogenous laboratory sample, but significantly larger in the field due to structural heterogeneities on different scales. Assuming the mechanical attributes (including the compaction energy, inelastic compaction and elastic moduli) are basically independent of scale, the model then predicts the

scaling relation (1) with an exponent $n = 0.5$, comparable to the field and laboratory data (Figure 8).

[43] The different scales of spatial heterogeneities would also control the stress magnitude required for compaction band propagation. From equations (2) and (3a) the remotely applied stress is given by

$$\sigma_{zz}^{\infty} = \frac{K}{\sqrt{\pi L}\sqrt{1 - (b/L)^2}} \tag{6}$$

This is a general relation that applies to all values of b/L, and as long as b/L is not very large we can also use (5a) and (5b) to arrive at this relatively simple expression for the stress necessary for compaction band propagation:

$$\sigma_{zz}^{\infty} = \sqrt{\frac{EG_c}{\pi(1 - \nu^2)L}} = \frac{2G_c}{\pi h} = \frac{2G_c}{\pi \varepsilon^p t_{max}} \tag{7}$$

[44] The anticrack/antidislocation model therefore predicts that the stress for compaction band propagation scales inversely with band thickness. Except for the geometric $\pi/2$, the above is identical to *Rudnicki and Sternlof's* [2005] result for a semi-infinite anticrack. We compile in Figure 10 the stress data (from Table 5 for laboratory deformed samples and inferred for Valley of Fire by *Sternlof et al.* [2005]) versus compaction band thickness on a log-log plot. The data are bracketed by lines of constant compaction energy G_c between 2 and 80 kJ/m^2, using a value of inelastic compactive strain of $\varepsilon^p = 0.14$ that has been estimated from our laboratory data in section 2.4. Assuming a plastic strain of $\varepsilon^p = 0.1$, *Rudnicki and Sternlof* [2005] arrived at similar estimates of G_c. In comparison, *Vajdova and Wong* [2003] obtained a lower bound on the compaction energy for Bentheim sandstone of 16 kJ/m^2, and *Tembe et al.* [2006] estimated G_c values ranging between 6 and 43 kJ/m^2 for Berea and Bentheim sandstones.

[45] Building upon *Rudnicki's* [2007] proposal that a combined anticrack/antidislocation model satisfactorily explains the observed quadratic relation between compaction band length and width, we demonstrate here that the same model predicts the stress to scale inversely with compaction band width, in agreement with laboratory data and inference from field observations. It should be emphasized that both scaling relations apply only if magnitude of the compaction energy does not vary significantly with spatial dimension, as postulated by *Rudnicki and Sternlof* [2005] as well as *Sternlof et al.* [2005]. Given that both the stress magnitude and damage intensity are inferred to be lower in the field, one may surmise that the compaction energy will also be considerably lower in these longer compaction bands. However, it should be kept in mind that compaction energy (defined to be the strain energy release per unit band area) corresponds to the totality of dissipated energy integrated over the lateral thickness of a compaction band, which is also thicker in the field.

4. Summary and Conclusion

[46] In this study we address several questions regarding the development and propagation of discrete compaction bands in porous sandstones, including the influence of composition and geometric attributes of the bands. We demonstrated from mechanical data and microstructural observation on the Diemelstadt and Bleurswiller arkosic sandstones that discrete compaction band can develop in a variety of sandstones. Discrete compaction bands were found to be the dominant failure mode in the transitional regime from brittle faulting to cataclastic flow in both the Diemelstadt and Bleurswiller. The geometric attributes of compaction bands produced in the arkosic sandstones were comparable to those in the Bentheim quartz sandstone, with lateral thicknesses of 0.5–0.6 mm. In the Diemelstadt, as in the Bentheim, mineralogical composition and water saturation did not appear to play an important role in the nucleation and growth of bands, which were subhorizontal and weakly tortuous.

[47] The geometric attributes of discrete compaction bands as observed in the laboratory are qualitatively similar to compaction bands documented in the field. However, discrepancies over the stress states involved and structure of the band limited further understanding of the phenomenon. Compiling laboratory and field data and incorporating recent theoretical developments provided quantitative means for relating the two. Data for five sandstones over length scales of $10^{-3} - 10$ m revealed that the thickness and length of compaction bands obey a quadratic scaling relation where the thickness scales approximately with the square root of the band length. On the basis of the anticrack/antidislocation fracture mechanics model we explored the mechanical interpretation for the broad range of stresses associated with compaction band propagation in the field and laboratory settings and obtained a scaling relation in which the stress level is inversely proportional to compaction band thickness. Thus for the laboratory bands, higher propagation stresses are predicted, as is the potential for significant damage, while for compaction bands in the field, lower stresses and less damage are expected. Together the laboratory and field data constrain the critical strain energy release rate in the model to be on the order of 2–80 kJ/m^2, comparable with laboratory estimates of the nominal compaction energy of 6–43 kJ/m^2.

References

Aydin, A., R. I. Borja, and P. Eichhubl (2006), Geological and mathematical framework for failure modes in granular rock, *J. Struct. Geol.*, *28*(1), 83–98.

Baud, P., W. Zhu, and T.-f. Wong (2000), Failure mode and weakening effect of water on sandstone, *J. Geophys. Res.*, *105*, 16,371–16,389.

Baud, P., E. Klein, and T.-f. Wong (2004), Compaction localization in porous sandstones: Spatial evolution of damage and acoustic emission activity, *J. Struct. Geol.*, *26*, 603–624.

Baud, P., V. Vajdova, and T.-f. Wong (2006), Shear-enhanced compaction and strain localization: Inelastic deformation and constitutive modeling of four porous sandstones, *J. Geophys. Res.*, *111*, B12401, doi:10.1029/2005JB004101.

Cowie, P. A., and C. H. Scholz (1992), Physical explanation for the displacement length relationship of faults using a post-yield fracture model, *J. Struct. Geol.*, *14*(10), 1133–1148.

DiGiovanni, A. A., J. T. Fredrich, D. J. Holcomb, and W. A. Olsson (2000), Micromechanics of compaction in an analogue reservoir sandstone, in *Proc. 4th North Am. Rock Mech. Symp.*, edited by J. Girard et al., pp. 1153–1160, Balkema, Seattle, WA.

Fletcher, R. C., and D. D. Pollard (1981), Anticrack model for pressure solution surfaces, *Geology*, *9*(9), 419–424.

Fortin, J., A. Schubnel, and Y. Guéguen (2005), Elastic wave velocities and permeability evolution during compaction of Bleurswiller sandstone, *Int. Rock Mech. Min. Sci.*, *42*(7–8), 873–889.

Fortin, J., S. Stanchits, G. Dresen, and Y. Guéguen (2006), Acoustic emission and velocities associated with the formation of compaction bands in sandstone, *J. Geophys. Res.*, *111*, B10203, doi:10.1029/2005JB003854.

Fortin, J., S. Guéguen, and Y. Schubnel (2007), Effects of pore collapse and grain crushing on ultrasonic velocities and V_p/V_s, *J. Geophys. Res.*, *112*, B08207, doi:10.1029/2005JB004005.

Fossen, H., and J. Hesthammer (1997), Geometric analysis and scaling relations of deformation bands in porous sandstones, *J. Struct. Geol.*, *19*(12), 1479–1493.

Hill, R. E. (1989), Analysis of deformation bands in the Aztec sandstone, Valley of Fire State Park, Nevada, master's thesis, Univ. of Nev., Las Vegas, Nev.

Holcomb, D. J., and W. A. Olsson (2003), Compaction localization and fluid flow, *J. Geophys. Res.*, *108*(B6), 2290, doi:10.1029/2001JB000813.

Issen, K. A., and J. W. Rudnicki (2000), Conditions for compaction bands in porous rock, *J. Geophys. Res.*, *105*, 21,529–21,536.

Kim, Y. S., and D. J. Sanderson (2005), The relationship between displacement and length of faults: A review, *Earth Sci. Rev.*, *68*, 317–334.

Klein, E. (2002), Micromécanique des roches granulaires poreuses: Expérimenation et modélisation, thèse de doctorat (in French), Univ. Louis Pasteur, Strasbourg, France.

Klein, E., and T. Reuschlé (2003), A model for the mechanical behaviour of Bentheim sandstone in the brittle regime, *Pure Appl. Geophys.*, *160*(5–6), 833–849.

Klein, E., and T. Reuschlé (2004), A pore crack model for the mechanical behaviour of porous granular rocks in the brittle deformation regime, *Int. J. Rock Mech. Min. Sci.*, *41*, 975–986.

Klein, E., P. Baud, T. Reuschlé, and T.-f. Wong (2001), Mechanical behaviour and failure mode of Bentheim sandstone under triaxial compression, *Phys. Chem. Earth (A)*, *26*, 33–38.

Louis, L., T.-f. Wong, P. Baud, and S. Tembe (2006), Imaging strain localization by X-ray computed tomography: Discrete compaction bands in Diemelstadt sandstone, *J. Struct. Geol.*, *28*, 762–775.

Menéndez, B., W. Zhu, and T.-f. Wong (1996), Micromechanics of brittle faulting and cataclastic flow in Berea sandstone, *J. Struct. Geol.*, *18*, 1–16.

Mollema, P. N., and M. A. Antonellini (1996), Compaction bands: A structural analog for anti-mode I cracks in Aeolian sandstone, *Tectonophysics*, *267*, 209–228.

Olsson, W. A. (1999), Theoretical and experimental investigation of compaction bands in porous rock, *J. Geophys. Res.*, *104*, 7219–7228.

Olsson, W. A., and D. J. Holcomb (2000), Compaction localization in porous rock, *Geophys. Res. Lett.*, *27*, 3537–3540.

Rudnicki, J. W. (2007), Models for compaction band propagation, in *Geomechanics and Rock Physics for Reservoir and Repository Characterization*, *Proceedings of Euroconference on Rock Physics 2005*, Spec. Publ., vol. 284, edited by C. David and M. Le Ravalec-Dupin, pp. 107–125, Geol. Soc., London, doi:10.1144/SP284.8.

Rudnicki, J. W., and K. R. Sternlof (2005), Energy release model of compaction band propagation, *Geophys. Res. Lett.*, *32*, L16303, doi:10.1029/2005GL023602.

Sternlof, K., J. W. Rudnicki, and D. D. Pollard (2005), Anticrack inclusion model for compaction bands in sandstone, *J. Geophys. Res.*, *110*, B11403, doi:10.1029/2005JB003764.

Tada, H., P. C. Paris, and G. R. Irwin (1973), *The Stress Analysis of Cracks Handbook*, Del Res. Corp., Hellertown, Pa.

Tembe, S., V. Vajdova, T.-f. Wong, and W. Zhu (2006), Initiation and propagation of strain localization in circumferentially notched samples of two porous sandstones, *J. Geophys. Res.*, *111*, B02409, doi:10.1029/2005JB003611.

Vajdova, V., and T.-f. Wong (2003), Incremental propagation of discrete compaction bands: Acoustic emission and microstructural observations on circumferentially notched samples of Bentheim sandstone, *Geophys. Res. Lett.*, *30*(14), 1775, doi:10.1029/2003GL017750.

Vajdova, V., P. Baud, and T.-f. Wong (2004), Permeability evolution during localized deformation in Bentheim sandstone, *J. Geophys. Res.*, *109*, B10406, doi:10.1029/2003JB002942.

Vos, M. W. (1990), Selection of outcrop samples for acoustic measurements on reservoir rock, Ph.D. thesis, Delft University of Technology, Netherlands.

Wong, T.-f., C. David, and W. Zhu (1997), The transition from brittle faulting to cataclastic flow in porous sandstones: Mechanical deformation, *J. Geophys. Res.*, *102*, 3009–3025.

Wong, T.-f., P. Baud, and E. Klein (2001), Localized failure modes in a compactant porous rock, *Geophys. Res. Lett.*, *28*, 2521–2524.

Zhang, J., T.-f. Wong, and M. D. Davis (1990a), Micromechanics of pressure induced grain crushing in porous rocks, *J. Geophys. Res.*, *95*, 341–352.

Zhang, J., T.-f. Wong, and, M. D. Davis (1990b), High pressure embrittlement and shear-enhanced compaction in Berea sandstone: Acoustic emission measurement and microstructural observation, in *Rock Mechanics Contributions and Challenges, Proceedings of 31st U.S. Symposium on Rock Mechanics*, edited by W. A. Hustrulid and G. A. Johnson, pp. 653–660, Balkema, Rotterdam.

————————————

P. Baud, Institut de Physique du Globe (CNRS/ULP), 5 rue Descartes, 67084 Strasbourg, France.

S. Tembe and T.-f. Wong, Department of Geosciences, State University of New York at Stony Brook, Stony Brook, NY 11794-2100, USA. (stembe@ic.sunysb.edu)